

Hierarchical porous metal ferrite ball-in-ball hollow spheres: General synthesis, formation mechanism, and high performance as anode materials for Li-ion batteries

Shouli Li, Aihua Li, Ranran Zhang, Yanyan He, Yanjun Zhai, and Liqiang Xu (✉)

Key Laboratory of Colloid and Interface Chemistry (Shandong University), Ministry of Education, and School of Chemistry and Chemical Engineering, Shandong University, Jinan 250100, China

Received: 25 January 2014

Revised: 8 April 2014

Accepted: 12 April 2014

© Tsinghua University Press
and Springer-Verlag Berlin
Heidelberg 2014

KEYWORDS

hierarchical,
porous,
ferrite,
lithium ion battery,
ball-in-ball

ABSTRACT

High yields of CoFe_2O_4 , NiFe_2O_4 and CdFe_2O_4 hierarchical porous ball-in-ball hollow spheres have been achieved using hydrothermal synthesis followed by calcination. The mechanism of formation is shown to involve an *in situ* carbonaceous-template process. Hierarchical porous CoFe_2O_4 hollow spheres with different numbers of shells can be obtained by altering the synthesis conditions. The electrochemical properties of the resulting CoFe_2O_4 electrodes have been compared, using different binders. The as-obtained CoFe_2O_4 and NiFe_2O_4 have relatively high reversible discharge capacity and good rate retention performance which make them promising materials for use as anode materials in lithium ion batteries.

1 Introduction

Hierarchical porous ball-in-ball hollow structured materials, which combine or integrate the advantages of both hollow spheres and porous shell architectures, have attracted tremendous and increasing attention owing to their low density, high porosity, high surface area, large pore volume and surface permeability. Materials with hierarchical porous ball-in-ball hollow structure characteristics have a wide variety of applications as catalysts and catalyst supports, com-

ponents of host–guest systems, for encapsulation of molecules or removal of waste, and as fillers for light weight or low density composites [1–4]. They have also been utilized as anode materials for lithium ion batteries (LIBs) since they can reduce transport lengths for both mass and charge transport and enhance structural integrity with sufficient void space to buffer the volume variation occurring during the Li^+ insertion/extraction process, leading to improved electrochemical performance [5–7]. Recently, a wide variety of examples of hierarchical porous, hollow or

Address correspondence to xulq@sdu.edu.cn

ball-in-ball structured metal oxides including V_2O_5 [8], ZnO [9], Co_3O_4 [10], Fe_2O_3 [11], NiO , CuO , SnO_2 , TiO_2 , $ZnFe_2O_4$ [12–15], $ZnMn_2O_4$, $MnFe_2O_4$ [16, 17] and $MnCo_2O_4$ [18] have been developed and shown to give improved performances in LIBs.

Metal ferrite materials have been among the most frequently chosen systems for studies of magnetism and have shown great potential for many important technological applications, ranging from information storage and electronic devices to medical diagnostics and drug delivery; they are also very good dielectric materials and energy storage materials. Very recently, ferrite materials with diverse morphologies such as films [19], flakes [20], hollow nanospheres [21], and macroporous particles [22] have been produced, and have been employed as anode materials which show enhanced properties in LIBs. However their discharge capacity usually fades rapidly below $700 \text{ mAh}\cdot\text{g}^{-1}$ and rate performances (especially at high charge/discharge rates) still need to be improved before they can be used in practical LIBs. There are at least two effective ways to improve their cycle performance: Either by hybrid or composite material design (such as $CoFe_2O_4$ /graphene and $ZnFe_2O_4$ /graphene nanocomposites) [23, 24], or morphology or structure control of the ferrites. However, developing a general strategy for the convenient high yield synthesis of a series of metal ferrites with hierarchical porous ball-in-ball hollow spherical structures which meet the requirements for practical applications as high performance anode materials for LIBs still remains a great challenge.

In this report, we introduce a general and facile approach for the high yield synthesis of series of metal ferrites including $CoFe_2O_4$, $NiFe_2O_4$ and $CdFe_2O_4$ with hierarchical porous ball-in-ball hollow spherical structures based on a hydrothermal method followed by a calcination step. Of these ferrites, the synthesis and electrochemical properties of $CoFe_2O_4$ and $NiFe_2O_4$ have been investigated in detail. The effects of different binders—polyvinylidene fluoride (PVDF) and carboxymethyl cellulose (CMC)—on the cycle performance of the $CoFe_2O_4$ have been investigated. The $CoFe_2O_4$ ball-in-ball double-shell hollow spheres display an initial discharge capacity of $1,151 \text{ mAh}\cdot\text{g}^{-1}$ at $100 \text{ mA}\cdot\text{g}^{-1}$ and deliver a reversible specific capacity as high as $895 \text{ mAh}\cdot\text{g}^{-1}$ after 70 cycles (close to the

theoretical capacity). It is interesting that porous $CoFe_2O_4$ hollow spheres with triple-shells could also be obtained simply by reducing the concentration of the sucrose solution to half of the original value. Both the $CoFe_2O_4$ and $NiFe_2O_4$ ball-in-ball hollow spheres have high rate performances, especially at high current densities. The high capacity and excellent rate performance of these ferrites are indicative of their high promise for application as anode materials in LIBs. Their formation processes are shown to involve an *in situ* carbonaceous-template process. In addition, hierarchical porous $CdFe_2O_4$ ball-in-ball double-shell hollow spheres could also be obtained in high yield through a similar route. Therefore, our method offers a general way for the high yield synthesis of hierarchical porous ferrite ball-in-ball hollow spheres, which might further promote their applications in wider areas.

2 Results and discussion

2.1 $CoFe_2O_4$

The morphology and structure of the $CoFe_2O_4$ double-shell product (S_1) were characterized by FESEM, HRTEM and XRD analyses (see Fig. 1). Figure 1(a) shows that a high yield of porous $CoFe_2O_4$ spheres (with an outer diameter of $0.5\text{--}1.5 \mu\text{m}$) composed of well inter-connected nanoscale particles was obtained. The TEM image in Fig. 1(b) shows that these porous $CoFe_2O_4$ spheres have the ball-in-ball hollow spherical characteristics with an inner core diameter of $200\text{--}500 \text{ nm}$ (a small hollow ball is stuck on one edge of the interior sphere to form interesting hierarchical complex structure, see Fig. 1(c)). Figure 1(e) displays the HRTEM image of the area marked by a square in Fig. 1(d); the clearly resolved lattice fringes with a lattice spacing of 0.48 nm are consistent with the (111) plane of cubic $CoFe_2O_4$. The EDS spectrum (Fig. 1(f)) further confirms the presence of Co, Fe and O elements. The X-ray diffraction pattern (XRD, Fig. 1(g)) shows sharp diffraction peaks with high intensity, indicating the high crystallinity of the product. All the diffraction peaks can be indexed as the single phase cubic $CoFe_2O_4$ (JCPDS Card No. 22-1086). The lattice constant calculated from this pattern is 8.381 \AA , which is close to the reported value. Figure 1(h) shows the structure

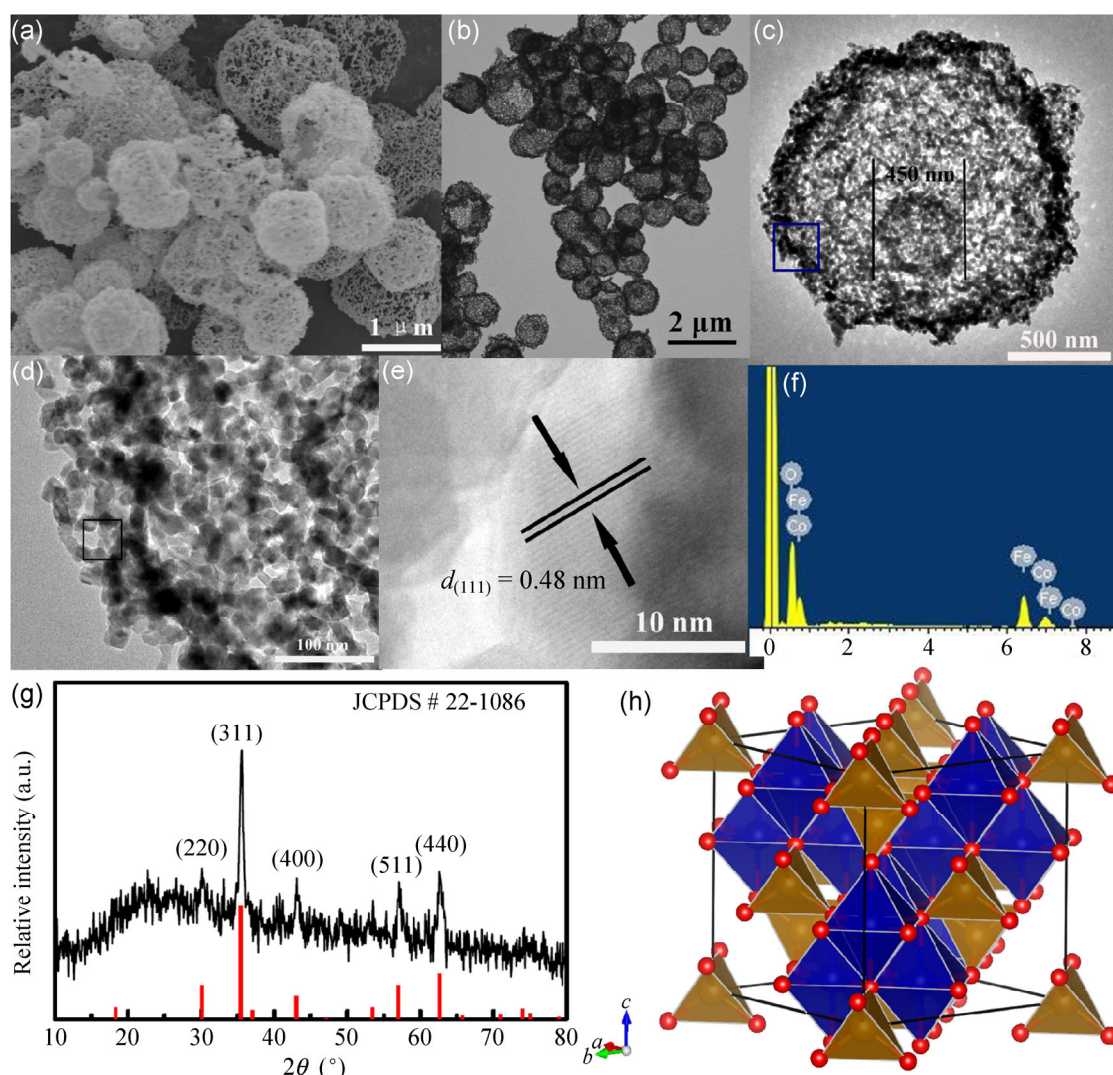


Figure 1 (a) FESEM, (b) TEM, (c)–(e) HRTEM images, (f) EDS spectrum, and (g) XRD pattern of the product S_1 ; (h) The schematic structure of CoFe_2O_4 generated using VESTA.

of the inverse spinel structure CoFe_2O_4 , in which the tetrahedral sites are occupied by Fe^{III} , while the octahedral sites are occupied by Fe^{III} and Co^{II} [25]. The above results indicate that hierarchical porous CoFe_2O_4 ball-in-ball hollow spheres, with high purity and high crystallinity, have been obtained in high yield.

It is interesting that simply by reducing the concentration of the sucrose solution to half of the original value, hierarchical porous CoFe_2O_4 ball-in-ball hollow spheres (S_2) with triple-shells are obtained in high yield (Figs. 2(a) and 2(b)), but some hierarchical porous spheres with double-shells and porous sphere-

hollow tube–sphere linked junctions are also formed (Figs. 2(c)–2(e)). Figure 2(f) presents the nitrogen adsorption–desorption isotherms and corresponding pore size distribution curve (inset in Fig. 2(f)) of S_2 . The adsorption–desorption hysteresis can be attributed to the formation of inhomogeneous mesopores (approximately 30 nm on average). The nitrogen sorption isotherm of the product exhibits a type IV curve with a H_3 hysteresis loop and with a specific surface area, obtained using the Brunauer–Emmett–Teller (BET) method, of about $38 \text{ m}^2 \cdot \text{g}^{-1}$. The pore size distribution curve further confirms the porous character of the product.

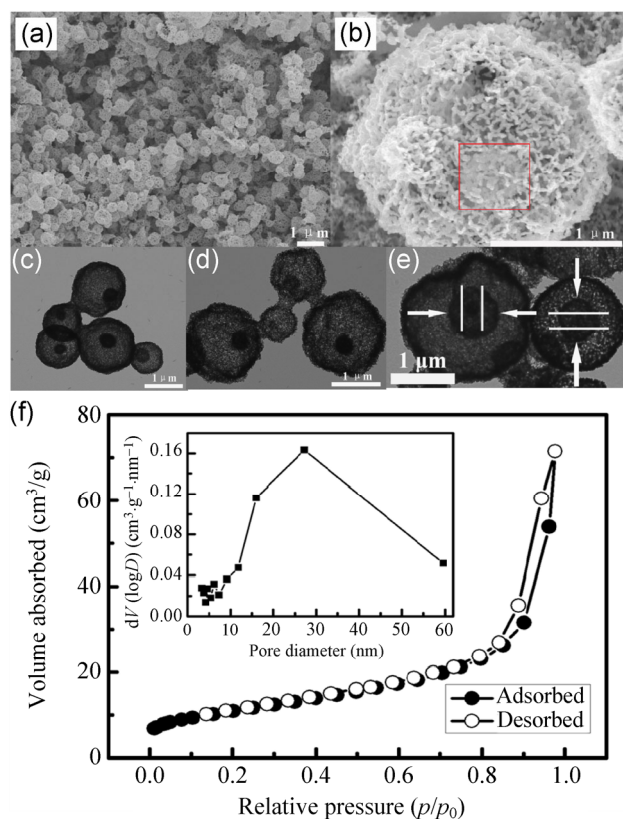


Figure 2 (a) and (b) FESEM images (the red square shows the existence of a small ball), and (c)–(e) TEM images of the CoFe_2O_4 product (S_2); (f) Typical nitrogen adsorption–desorption isotherms of the product S_2 .

In order to explore whether the CoFe_2O_4 spheres can be employed in LIBs or not, the cyclic voltammogram (CV) of the S_1 electrode for the first five cycles were obtained (Fig. 3(a)). The reduction peak centered at 0.61 V in the first cycle corresponds to the redox reactions of CoFe_2O_4 with Li giving metallic Fe, Co and Li_2O , accompanied by the decomposition of the electrolyte to form a solid electrolyte interphase (SEI) layer [1], while the subsequent sweeps show two reduction peaks centered at ~0.84 V and 1.56 V, which are related to the reduction of Fe_2O_3 and CoO to metallic Fe and Co, respectively [3]. The decrease in reduction peak intensity indicates that the capacity decreases after the first cycle. In the oxidation cycle, a main broad peak centered at 1.78 V is attributed to the oxidation of metallic iron to $\text{Fe}(\text{III})$ and cobalt to $\text{Co}(\text{II})$. After the first cycle, the anodic peaks shift to ~1.80 V, which may be related to the partial polarization of the CoFe_2O_4 sample [2]. It should be noted that the

peak intensity and integrated area during the reductive and oxidative polarization processes remained almost unchanged after the first scan cycle, indicating the good electrochemical reversibility of the as-obtained CoFe_2O_4 spheres. The effects of different binders on the electrochemical properties and cycle performance of the CoFe_2O_4 sphere electrode were evaluated. Figures 3(b)–3(d) display selected charge and discharge cycle profiles and rate capability of the CoFe_2O_4 electrode using PVDF as a binder. The difference in the voltage profiles of CoFe_2O_4 between the first discharge process and the subsequent cycles indicates that different redox reactions are occurring. The first discharge curve exhibits one plateau at 0.75 V, while the subsequent discharge curve plateaus are slightly higher than the first one, which is consistent with the CV results. The first discharge and charge capacities of the product respectively reach 1,202 and 889 $\text{mAh}\cdot\text{g}^{-1}$ at a current density of 100 $\text{mA}\cdot\text{g}^{-1}$, corresponding to a coulombic efficiency of 74%. The extra capacity can be ascribed to the formation of SEI films and electrolyte decomposition [26]. Figure 3(c) displays the corresponding cycling performance of the $\text{CoFe}_2\text{O}_4/\text{Li}$ button battery at 100 $\text{mA}\cdot\text{g}^{-1}$. After 70 cycles, the specific capacity remains as high as 758 $\text{mAh}\cdot\text{g}^{-1}$ and the coulombic efficiency of each cycle is above 92%. The rate capacity of CoFe_2O_4 was studied at different current densities (100–2,000 $\text{mA}\cdot\text{g}^{-1}$). The button battery shows relatively good rate capability (Fig. 3(d)) with the lowest discharge capacities of 913, 681, 529, 432 and 309 $\text{mAh}\cdot\text{g}^{-1}$, at rates of 100, 200, 500, 1,000 and 2,000 $\text{mA}\cdot\text{g}^{-1}$, respectively. Upon altering the current density back to 100 $\text{mA}\cdot\text{g}^{-1}$, the discharge capacity recovered to 907 $\text{mAh}\cdot\text{g}^{-1}$. Figures 3(e) and 3(h) present the cycle stability, discharge/charge profiles and rate capability of the CoFe_2O_4 electrode using CMC as the binder for comparison. Its first discharge capacity is 1,151.8 $\text{mAh}\cdot\text{g}^{-1}$ at 100 $\text{mA}\cdot\text{g}^{-1}$ (with a coulombic efficiency of 80.4%) and its specific capacity remains at 895.2 $\text{mAh}\cdot\text{g}^{-1}$ (which is close to the theoretical capacity) after 70 cycles. The coulombic efficiency of each cycle is above 94%, except for the first two cycles. The cell displays good rate capability and stable cycle performances with average discharge capacity of 896, 768, 641, 542 and 406 $\text{mAh}\cdot\text{g}^{-1}$ at current densities of 100, 200, 500, 1,000 and 2,000 $\text{mA}\cdot\text{g}^{-1}$, respectively.

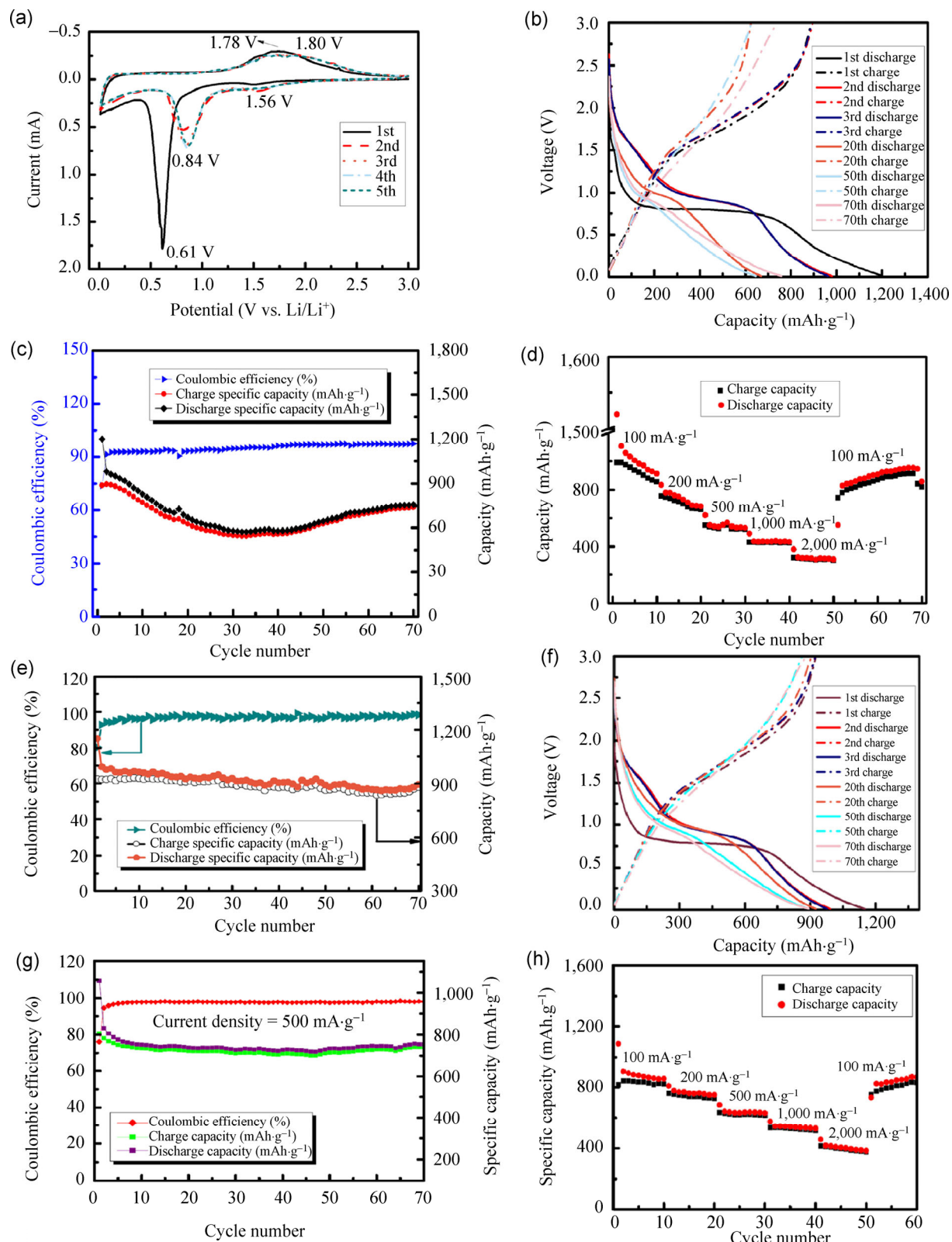


Figure 3 Electrochemical performance of the CoFe_2O_4 electrode using (a)–(d) PVDF or using (e)–(h) CMC as the binder: (a) CV curves; (b)–(d) Cycle performance and rate performances of the electrode; (e) and (h) Capacity, coulombic efficiency and discharge/charge profiles of the electrode as a function of cycle number at $100 \text{ mA}\cdot\text{g}^{-1}$; (g) Cycle performance of the electrode at $500 \text{ mA}\cdot\text{g}^{-1}$; (h) Rate performances of the electrode.

The capacity of the CoFe_2O_4 electrode is comparable to that of commercially used graphite (372 $\text{mAh}\cdot\text{g}^{-1}$) even at a current density of 2,000 $\text{mA}\cdot\text{g}^{-1}$. The higher reversible capacity and better rate capability of the electrodes (using CMC as a binder) can be mainly attributed to the stronger binding ability of CMC (stabilizing the whole electrode to a higher degree) compared with that of PVDF, giving it great potential for application as a high rate anode material in lithium ion batteries. The cycle stability of the CoFe_2O_4 ball-in-ball hollow spheres was also studied by dismantling the cell after 20 cycles at 500 $\text{mA}\cdot\text{g}^{-1}$. It was found that the majority of the CoFe_2O_4 spheres (Figs. S1(a)–S1(c) in the Electronic Supplementary Material (ESM)) retain their original shape, indicating their attractive structural stability, while the discharge capacities of the solid CoFe_2O_4 spheres (Fig. S2(a) in the ESM) and hollow CoFe_2O_4 spheres (prepared after calcination at 450 °C, Fig. S2(b) in the ESM) were only 301 and 547 $\text{mAh}\cdot\text{g}^{-1}$, after 70 and 55 cycles, respectively. The long cycle stability and high discharge capacity of the as-obtained hierarchical porous CoFe_2O_4 ball-in-ball hollow spheres approach those of CoFe_2O_4 /graphene nanocomposites [23] and are higher than the corresponding values for an ordered macroporous CoFe_2O_4 material [22], indicating their promise for application as an anode for LIBs.

2.2 NiFe_2O_4

Figure 4(a) displays the XRD pattern of the NiFe_2O_4 product obtained by using $\text{NiSO}_4\cdot 6\text{H}_2\text{O}$ as the nickel source in the hydrothermal process with a subsequent calcination step at a temperature of 700 °C. All the diffraction peaks can be indexed as the single phase cubic NiFe_2O_4 (JCPDS Card No. 74-1913). The sharp diffraction peaks with high intensity reveals the good crystallinity of the product. The TEM, FESEM and HRTEM images of the NiFe_2O_4 product are shown in Figs. 4(b)–4(f). NiFe_2O_4 with a hierarchical porous ball-in-ball hollow spherical structure and high crystallinity was obtained in high yield. The electrochemical properties of the hierarchical porous NiFe_2O_4 ball-in-ball hollow spheres are exhibited in Fig. 5. Figure 5(a) presents the discharge/charge curves of the NiFe_2O_4 electrode at a current density of 200 $\text{mA}\cdot\text{g}^{-1}$ at room temperature in a potential window between 0.01

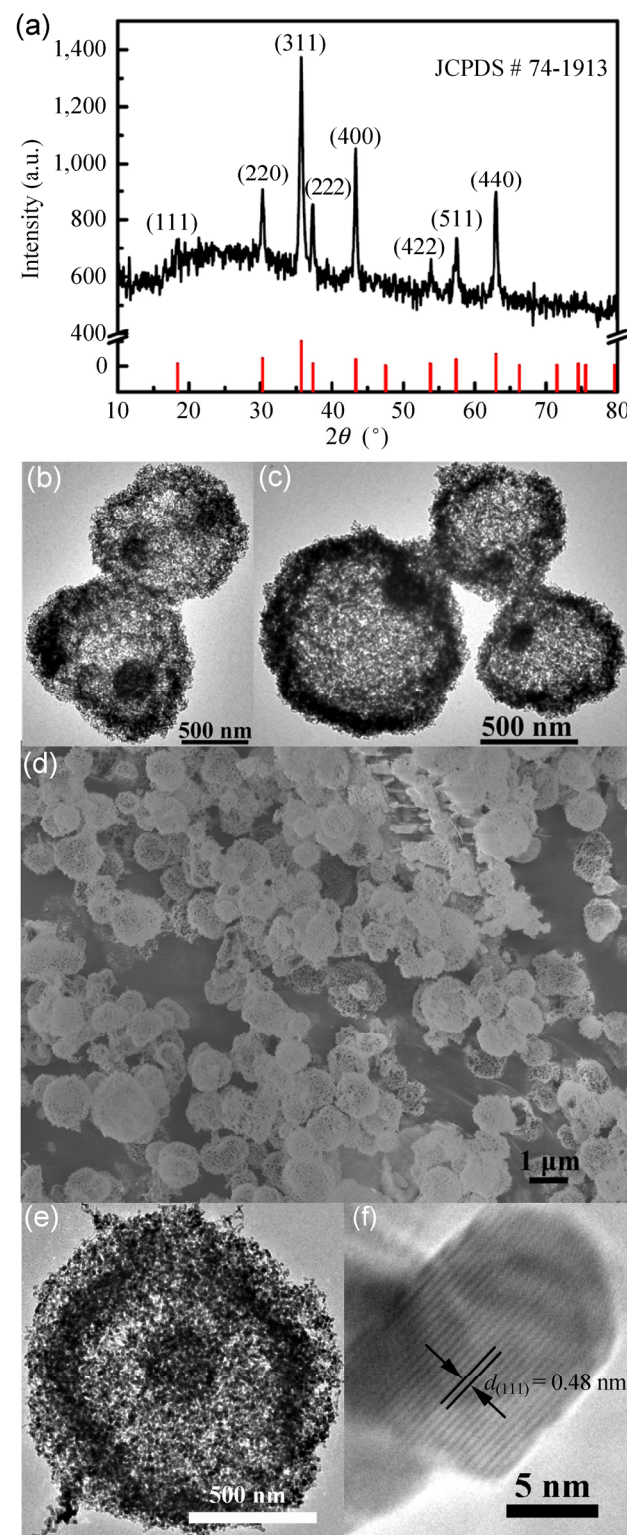


Figure 4 (a) XRD pattern, (b)–(f) TEM, FESEM and HRTEM images of hierarchical porous NiFe_2O_4 ball-in-ball hollow spheres obtained using $\text{NiSO}_4\cdot 6\text{H}_2\text{O}$ as the nickel source and subsequent calcination at 700 °C.

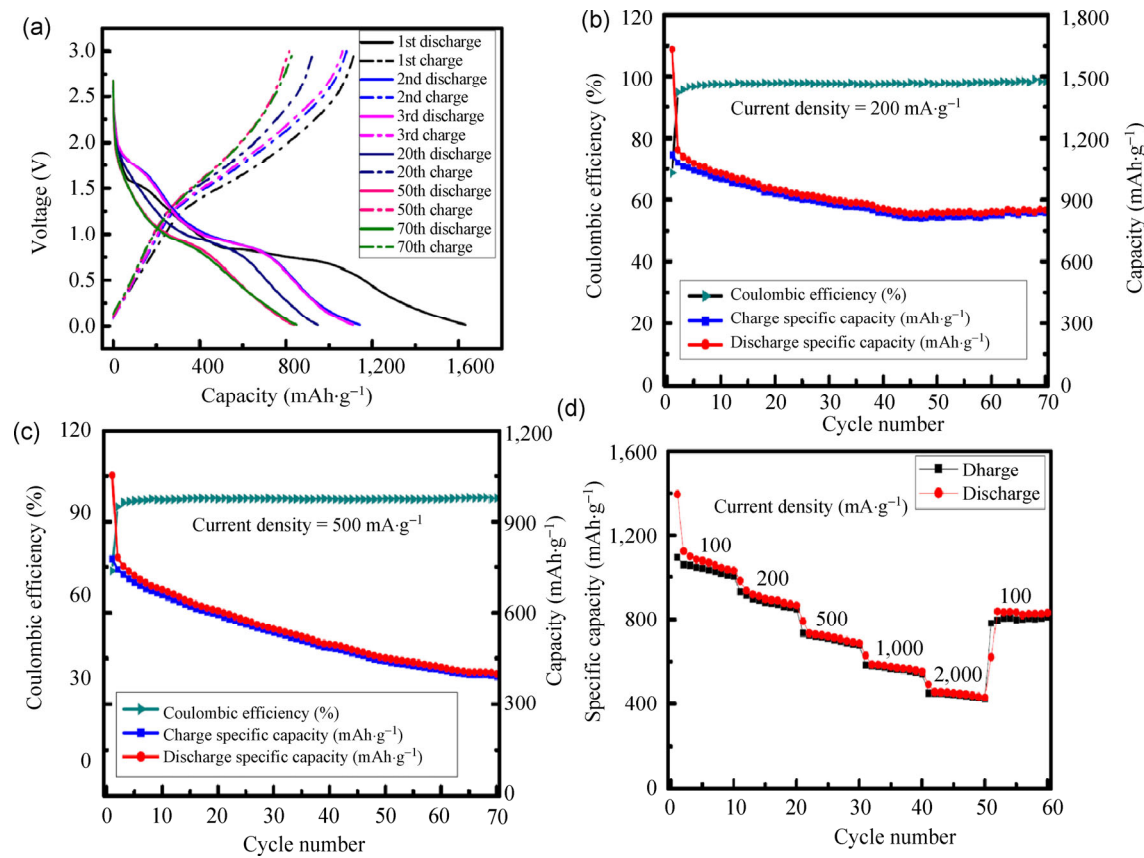


Figure 5 Electrochemical performance of the NiFe_2O_4 electrode (with CMC as the binder): (a) and (b) Discharge/charge profiles, capacity and coulombic efficiency as a function of cycle number at a current density of $200 \text{ mA}\cdot\text{g}^{-1}$; (c) Capacity and coulombic efficiency as a function of cycle number at a current density of $500 \text{ mA}\cdot\text{g}^{-1}$; (d) Rate performance of the electrode.

and 3.0 V (vs. Li^+/Li). It can be seen that the initial discharge/charge specific capacities are as high as $1,632/1,119.5 \text{ mAh}\cdot\text{g}^{-1}$; these values are higher than those previously reported for NiFe_2O_4 nanorods [27]. Figure 5(b) shows the discharge/charge capacity versus cycle number for the NiFe_2O_4 electrode at a current density of $200 \text{ mA}\cdot\text{g}^{-1}$. The capacity of the NiFe_2O_4 electrode is quite stable with only a slight fading in the first 50 cycles. After that, the discharge capacity remains stable in the range $840\text{--}850 \text{ mAh}\cdot\text{g}^{-1}$, and a reasonably high capacity of $850.4 \text{ mAh}\cdot\text{g}^{-1}$ can be obtained after 70 cycles. Although there is an obvious capacity decrease, the discharge capacity of the NiFe_2O_4 electrode remained at $580 \text{ mAh}\cdot\text{g}^{-1}$ at $500 \text{ mA}\cdot\text{g}^{-1}$ after 25 cycles (and $\sim 400 \text{ mAh}\cdot\text{g}^{-1}$ after 70 cycles, see Fig. 5(c)), which is higher than the value for solid NiFe_2O_4 spheres obtained by calcination at 500°C ($520 \text{ mAh}\cdot\text{g}^{-1}$ after 25 cycles, see Fig. S2(c) in the ESM). The rate

performance of the NiFe_2O_4 electrode cycled at various current densities is shown in Fig. 5(d). The reversible capacity stabilized at $1,030.4$, 868.6 , 686.9 , 553.7 and $432.4 \text{ mAh}\cdot\text{g}^{-1}$ upon increasing the discharge/charge current density to 100 , 200 , 500 , $1,000$ and $2,000 \text{ mA}\cdot\text{g}^{-1}$, respectively. However, when the current density was returned to $100 \text{ mA}\cdot\text{g}^{-1}$, the capacity recovered to $832.1 \text{ mAh}\cdot\text{g}^{-1}$. Both the cycle performance and rate performance indicate the good reversibility and stability of NiFe_2O_4 electrode, which are important factors for future possible applications in areas such as electric vehicles and portable power tools. In addition, it was found that the electrode material (NiFe_2O_4 /acetylene black/CMC) remained attached to the copper foil after 20 cycles at $500 \text{ mA}\cdot\text{g}^{-1}$. The majority of the NiFe_2O_4 spheres (Figs. S1(d) and S1(e) in the ESM) retain spherical characteristics after 20 cycles at $500 \text{ mA}\cdot\text{g}^{-1}$, showing the higher structural stability



of the ball-in-ball NiFe_2O_4 spheres compared with that of the hollow spheres (Fig. S1(f) in the ESM).

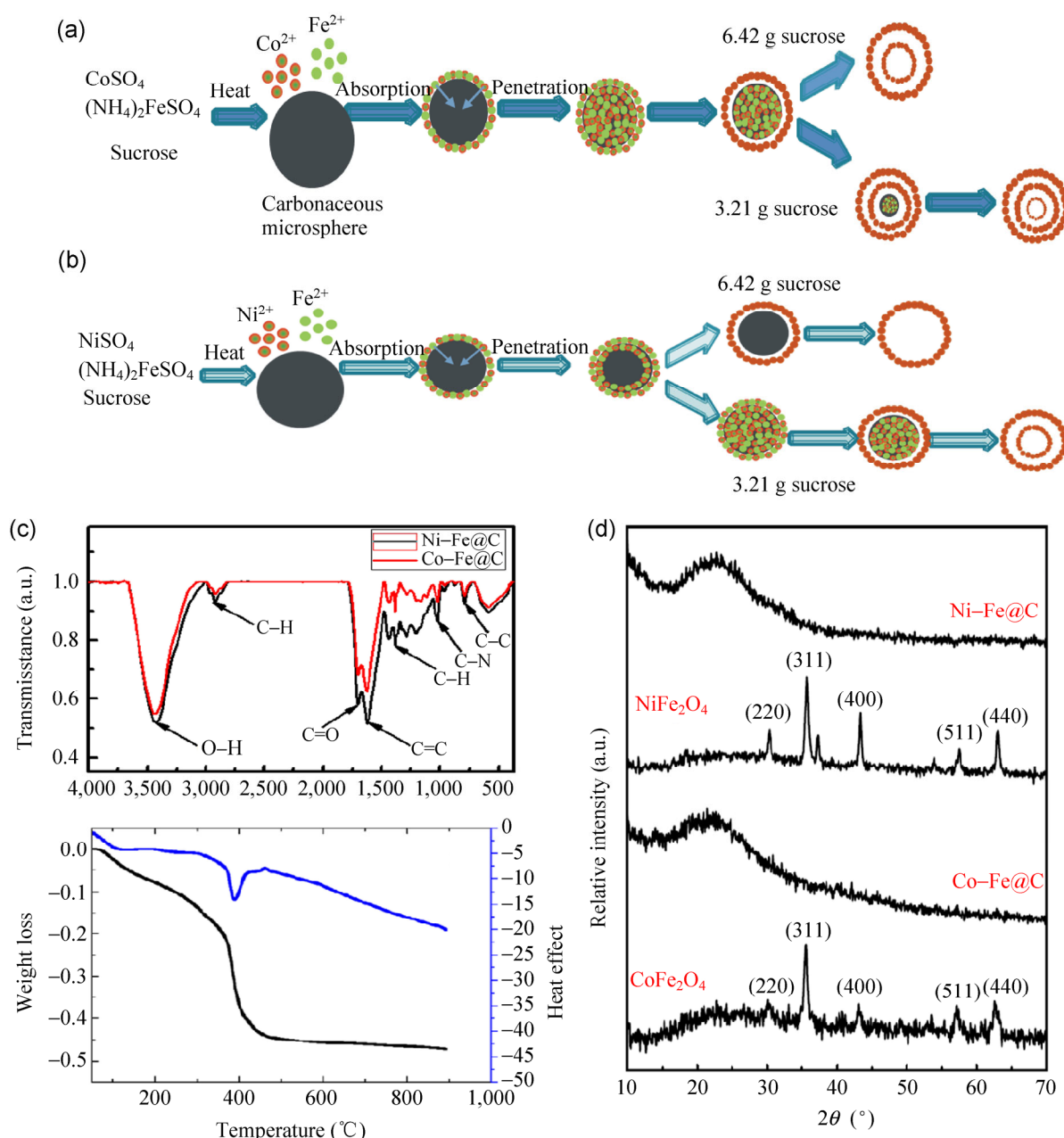
2.3 Formation processes of the hierarchical porous CoFe_2O_4 and NiFe_2O_4 ball-in-ball hollow spheres

The formation processes of the hierarchical porous CoFe_2O_4 and NiFe_2O_4 ball-in-ball hollow spheres were investigated. In the synthesis, sucrose is a “green” solvent which possesses good coordinating ability and can act as a ligand to form coordination complexes with cobalt ions (or nickel and other metal ions) upon heating. As the solution approached a critical supersaturation, nucleation occurred (thermal decomposition of metal coordination complexes and carbonization of sucrose). To reduce the total surface energy, some of the metal ions become encapsulated in the initial small carbonaceous spheres. With prolonged reaction time and increasing pressure within the sealed autoclave, other ions are subsequently adsorbed on the surface or/and penetrate into the larger spheres to form composites driven by electrostatic and magnetic interactions and coordination with functional groups (such as surface hydroxyl groups). Upon calcination, hierarchical porous CoFe_2O_4 and NiFe_2O_4 ball-in-ball hollow spheres are finally formed along with the gradual oxidation of graphite, and the final formation of a porous structure can be correlated with the release of gases such as oxygen or hydrogen and water during the whole processes. The formation processes is believed to involve an *in situ* carbonaceous-template process (see Schemes 1(a) and 1(b)). The above analysis is partly supported by the FTIR spectra, TGA curves (Schemes 1(c)–1(e)), TEM images (see Figs. S3 and S4 in the ESM) and XRD patterns (evolution from amorphous to crystalline) of the raw and final products (Schemes 1(c)–1(e)). The interior core (the solid carbonaceous sphere formed by decomposition of sucrose) is believed to act as an *in situ* carbonaceous-template during the final formation (after calcination) of the hierarchical porous hollow structure ferrites with double- or triple-shells (Figs. S3(b)–S3(d) in the ESM). It was found that when glucose was used instead of sucrose while keeping other conditions unchanged, hierarchical porous CoFe_2O_4 ball-in-ball hollow spheres still could also be obtained (Fig. S5 in the ESM). A relatively low rate of temperature increase

during calcination (1 °C per minute, as shown in Fig. S6 in the ESM) favors the production of hierarchical porous NiFe_2O_4 ball-in-ball hollow spheres with higher yield than when the temperature was increased more rapidly (4 °C per minute, see Fig. S7 in the ESM). In addition, the formation of the ball-in-ball hollow spheres depends on the calcination temperature: For example, a higher temperature favors the formation of hierarchical hollow ball-in-ball spheres (Fig. S2(h) in the ESM shows the TEM image of one sphere after calcination at 700 °C), while a lower temperature leads to the production of solid spheres (Figs. S2(f) and S2(g) in the ESM are TEM images of solid spheres obtained after calcination at 300 and 500 °C). It is worth noting that this approach can be extended to prepare other metal oxide materials with similar structure characteristics, such as CdFe_2O_4 (Fig. S8 in the ESM). Therefore, our approach offers a general way for the convenient fabrication of other ferrites with hierarchical porous ball-in-ball hollow spherical structures.

3 Conclusions

Hierarchical porous CoFe_2O_4 , NiFe_2O_4 and CdFe_2O_4 ball-in-ball hollow spheres having high crystallinity have been conveniently prepared in high yields using a hydrothermal method with a subsequent calcination process, and the synthesis has been shown to involve an *in situ* carbonaceous-template process. The controllable fabrication of hierarchical porous CoFe_2O_4 hollow spheres with different numbers of shells and the use of different binders has allowed the electrochemical properties of the resulting CoFe_2O_4 electrodes to be compared. The as-obtained CoFe_2O_4 and NiFe_2O_4 exhibit excellent rate performance and high reversible specific capacity. The improved performances of the products compared with those in the previous reports can mainly be attributed to their unique structures: Firstly, the inter-connected nanoparticles composed of porous network-like shells provide a short pathway for Li^+ diffusion; secondly, the ball-in-ball hollow structure facilitates the penetration of the electrolyte and buffers the volume changes during charge/discharge cycling processes; thirdly, the hierarchical porous architecture with a spherical



Scheme 1 (a) and (b) Schematic formation processes of the hierarchical porous ball-in-ball hollow structured CoFe₂O₄ and NiFe₂O₄ materials; (c) FTIR spectra and (d) XRD patterns of the CoFe₂O₄ and NiFe₂O₄ products obtained before and after calcination; (e) TGA curve of the as-obtained raw CoFe₂O₄ sample without calcination. The dramatic weight loss of the product is mainly attributed to the loss of graphite that originates from sucrose.

structure possesses relatively low surface energy, which results in less self-aggregation during cycling processes. The good performances of the products make them promising materials for application as a high capacity and high power anode material in LIBs. Our approach is believed to provide a general way

for the convenient fabrication of metal ferrites with similar structural characteristics, and can be expected to stimulate structure design, property tailoring and potential applications of these novel materials in broader research areas such as supercapacitors and catalyst-related materials.

4 Experimental

4.1 Fabrication of hierarchical porous CoFe_2O_4 ball-in-ball hollow spheres

All the reagents were analytical grade and used without further purification. In a typical procedure, 0.356 g of $\text{CoSO}_4 \cdot 7\text{H}_2\text{O}$ and 0.985 g of $(\text{NH}_4)_2\text{Fe}(\text{SO}_4)_2 \cdot 6\text{H}_2\text{O}$ were dissolved in 10 mL of ultrapure water; 6.42 g of sucrose was dissolved in 20 mL of ultrapure water to form another solution. Then the two solutions were simultaneously transferred into a Teflon-lined stainless steel autoclave with a capacity of about 45 mL and stirred for some time. The autoclave was sealed and maintained at 180 °C for 24 h. After it was cooled down to room temperature, the precipitate was isolated by filtration and washed several times with distilled water and absolute ethanol. Finally, the product was dried in a vacuum oven at 80 °C for 5 h. Finally, the product was calcined at 600 °C for 2 h in an electronic furnace with a heating rate of 4 °C·min⁻¹. The product is denoted “S₁”. When the sucrose solution concentration was adjusted to half of the original value, a product with different morphology was obtained and denoted “S₂”.

4.2 Fabrication of other hierarchical porous ferrite ball-in-ball hollow spheres

For the synthesis of NiFe_2O_4 , $\text{NiSO}_4 \cdot 6\text{H}_2\text{O}$ was used as nickel source and the calcination temperature was set at 700 °C. For the synthesis of CdFe_2O_4 , $\text{CdSO}_4 \cdot 8\text{H}_2\text{O}$ was used as the cadmium source and the calcination temperature was set at 600 °C while keeping the other experimental conditions unchanged.

4.3 Characterization

X-ray diffraction (XRD) patterns were obtained using a Bruker D8 Advance X-ray diffractometer with Cu K α radiation ($\lambda = 1.5418 \text{ \AA}$). TEM images were taken on a JEM-2100 transmission electron microscope. The high resolution images were recorded using a high resolution transmission electron microscope (HRTEM, JEOL-2010) operating at 200 kV. Particle morphology images were recorded using a field-emission scanning

electron microscope (FESEM, JEOL JSM-6700 M). The BET surface area and Barrett–Joyner–Halenda (BJH) pore size distribution (PSD) were characterized using a QuadraSorb SI surface area analyzer (version 5.06).

4.4 Electrochemical property investigation

The electrochemical performance of the samples versus Li was characterized using 2,032 coin cells. The anode materials were prepared by mixing the sample (60 wt.%) with acetylene black (30 wt.%) and polyvinylidene fluoride (PVDF) (10 wt.%) in *N*-methylpyrrolidone (NMP) to ensure homogeneity. In other cases, carboxymethyl cellulose (CMC) was used as a binder in place of PVDF and water was used as the solvent. After the slurry was milled (QM-3SP2 Planetary Ball Mill) for 3 h, it was coated on a piece of Cu foil with a thickness of 200 μm and dried under vacuum at 80 °C for 12 h. Then, the electrode materials coated on Cu foil were cut into circular discs of 12 mm in diameter. The average weight of the electrode was in the range 1.5–2.0 mg (excluding the Cu foil). The electrochemical coin cells were assembled in a glove box filled with high-purity argon with the pressures of oxygen and water both lower than 1 ppm. Li foil was used as the counter electrode, Ni foam as the current collector and a Celgard 2300 microporous membrane as a separator. The electrolyte was a 1 mol·L⁻¹ solution of LiPF₆ in ethylene carbonate/dimethyl carbonate/diethyl carbonate (EC/DMC/DEC) with a volume ratio of 1:1:1. Galvanostatic charge/discharge tests were conducted using a Land battery test system (CT2001A, China) at room temperature (25 °C). The cyclic voltammetry (CV) profiles were measured using a LK2005A Electrochemical Workstation in the region 0.01–3.0 V at a scan rate of 0.1 mV·s⁻¹.

Acknowledgements

Financial support from National Nature Science Foundation of China and the Academy of Sciences Large Apparatus United Fund (No. 11179043), and the 973 Project of China (No. 2011CB935901) are greatly appreciated.

Electronic Supplementary Material: Supplementary material (further details of the annealing and oxidation procedures, STM measurements, AFM imaging and Raman spectroscopy measurements) is available in the online version of this article at <http://dx.doi.org/10.1007/s12274-014-0474-3>.

References

- 1] Oh, M. H.; Yu, T.; Yu, S.-H.; Lim, B.; Ko, K.-T.; Willinger, M.-G.; Seo, D.-H.; Kim, B.-H.; Cho, M. G.; Parm, J.-H., et al. Galvanic replacement reactions in metal oxide nanocrystals. *Science* **2013**, *340*, 964–968.
- 2] Cho, N.-H.; Cheong, T.-C.; Min, J. H.; Wu, J. H.; Lee, S. J.; Kim, D.; Yang, J.-S.; Kim, S.; Kim Y. K.; Seong, S.-Y. A multifunctional core–shell nanoparticle for dendritic cell-based cancer immunotherapy. *Nat. Nanotechnol.* **2011**, *6*, 675–681.
- 3] Park, J.; Zheng, H. M.; Jun, Y.-W.; Alivisatos, A. P. Heteroepitaxial anion exchange yields single-crystalline hollow nanoparticles. *J. Am. Chem. Soc.* **2009**, *131*, 13943–13945.
- 4] Zhang, Q.; Wang, W. S.; Goebel, J.; Yin, Y. D. Self-templated synthesis of hollow nanostructures. *Nano Today* **2009**, *4*, 494–507.
- 5] Pan, A. Q.; Wu, H. B.; Zhang, L.; Lou, X. W. Uniform V_2O_5 nanosheet-assembled hollow microflowers with excellent lithium storage properties. *Energy Environ. Sci.* **2013**, *6*, 1476–1479.
- 6] Wang, Z. Y.; Zhou, L.; Lou, X. W. Metal oxide hollow nanostructures for lithium-ion batteries. *Adv. Mater.* **2012**, *24*, 1903–1911.
- 7] Wang, J. Y.; Yang, N. L.; Tang, H. J.; Dong, Z. H.; Jin, Q.; Yang, M.; Kisailus, D.; Zhao, H. J.; Tang Z. Y.; Wang, D. Accurate control of multishelled Co_3O_4 hollow microspheres as high-performance anode materials in lithium-ion batteries. *Angew. Chem. Int. Ed.* **2013**, *52*, 6417–6420.
- 8] Lai, X. Y.; Halpert, J. E.; Wang, D. Recent advances in micro-/nano-structured hollow spheres for energy applications: From simple to complex systems. *Energy Environ. Sci.* **2012**, *5*, 5604–5618.
- 9] Dong, Z. H.; Lai, X. Y.; Halpert, J. E.; Yang, N. L.; Yi, L. X.; Zhai, J.; Wang, D.; Tang, Z. Y.; Jiang, L. Accurate control of multishelled ZnO hollow microspheres for dye-sensitized solar cells with high efficiency. *Adv. Mater.* **2012**, *24*, 1046–1049.
- 10] Lou, X. W.; Archer, L. A.; Yang, Z. C. Hollow micro-/nanostructures: Synthesis and applications. *Adv. Mater.* **2008**, *20*, 3987–4019.
- 11] Son, M. Y.; Hong, Y. J.; Lee J.-K.; Kang, Y. C. One-pot synthesis of Fe_2O_3 yolk–shell particles with two, three, and four shells for application as an anode material in lithium-ion batteries. *Nanoscale* **2013**, *5*, 11592–11597.
- 12] Li, Z. M.; Lai, X. Y.; Wang, H.; Mao, D. Xing, C. J.; Wang, D. General synthesis of homogeneous hollow core–shell ferrite microspheres. *J. Phys. Chem. C* **2009**, *113*, 2792–2797.
- 13] Zhang, G. Q.; Yu, L.; Wu, H. B.; Hoster, H. E.; Lou, X. W. Formation of $ZnMn_2O_4$ ball-in-ball hollow microspheres as a high-performance anode for lithium-ion batteries. *Adv. Mater.* **2012**, *24*, 4609–4613.
- 14] Lou, X. W.; Wang, Y.; Yuan, C. L.; Lee, J. Y.; Archer, L. A. Template-free synthesis of SnO_2 hollow nanostructures with high lithium storage capacity. *Adv. Mater.* **2006**, *18*, 2325–2329.
- 15] Li, Y.; Fu, Z.-Y.; Su, B.-L. Hierarchically structured porous materials for energy conversion and storage. *Adv. Funct. Mater.* **2012**, *22*, 4634–4667.
- 16] Hu, J.; Chen, M.; Fang, X. S.; Wu, L. M. Fabrication and application of inorganic hollow spheres. *Chem. Soc. Rev.* **2011**, *40*, 5472–5491.
- 17] Song, Q.; Zhang, Z. J. Controlled synthesis and magnetic properties of bimagnetic spinel ferrite $CoFe_2O_4$ and $MnFe_2O_4$ nanocrystals with core–shell architecture. *J. Am. Chem. Soc.* **2012**, *134*, 10182–10190.
- 18] Li, J. F.; Wang, J. Z.; Liang, X.; Zhang, Z. J.; Liu, H. K.; Qian, Y. T.; Xiong, S. L. Hollow $MnCo_2O_4$ submicrospheres with multilevel interiors: From mesoporous spheres to yolk-in-double-shell structures. *ACS Appl. Mater. Interfaces* **2014**, *6*, 24–30.
- 19] Chu, Y.-Q.; Fu Z.-W.; Qin, Q.-Z. Cobalt ferrite thin films as anode material for lithium ion batteries. *Electrochim. Acta* **2004**, *49*, 4915–4921.
- 20] Lavela, P.; Tirado, J. L. $CoFe_2O_4$ and $NiFe_2O_4$ synthesized by sol–gel procedures for their use as anode materials for Li ion batteries. *J. Power Sources* **2007**, *172*, 379–387.
- 21] Wang, Y.; Su, D. W.; Ung, A.; Ahn J.-H.; Wang, G. X. Hollow $CoFe_2O_4$ nanospheres as a high capacity anode material for lithium ion batteries. *Nanotechnology* **2012**, *23*, 055402.
- 22] Li, Z. H.; Zhao, T. P.; Zhan, X. Y.; Gao, D. S.; Xiao, Q. Z.; Lei, G. T. High capacity three-dimensional ordered macroporous $CoFe_2O_4$ as anode material for lithium ion batteries. *Electrochim. Acta* **2010**, *55*, 4594–4598.
- 23] Xia, H.; Zhu, D. D.; Fu, Y. S.; Wang, X. $CoFe_2O_4$ –graphene nanocomposite as a high-capacity anode material for lithium-ion batteries, *Electrochim. Acta* **2012**, *83*, 166–174.

[24] Liu, S. Y.; Xie, J.; Fang, C. C.; Cao, G. S.; Zhu T. J.; Zhao, X. B. Self-assembly of a CoFe₂O₄/graphene sandwich by a controllable and general route: Towards a high-performance anode for Li-ion batteries. *J. Mater. Chem.* **2012**, *22*, 19738–19743.

[25] Momma, K.; Izumi, F. *VESTA*: A three-dimensional visualization system for electronic and structural analysis. *J. Appl. Cryst.* **2008**, *41*, 653–658.

[26] Wei, W.; Wang, Z. H.; Liu, Z. ; Liu, Y.; He, L. ; Chen, D. Z.; Umar, A.; Guo, L.; Li, J. H. Metal oxide hollow nanostructures: Fabrication and Li storage performance. *J. Power Sources* **2013**, *238*, 376–387.

[27] Wang, N. N.; Xu, H. Y.; Chen, L.; Gu, X.; Yang J.; Qian, Y. T. A general approach for MFe₂O₄ (M = Zn, Co, Ni) nanorods and their high performance as anode materials for lithium ion batteries. *J. Power Sources* **2014**, *247*, 163–169.